Q. J. R. Meteorol. Soc. (2005), **131**, pp. 1113–1128 doi: 10.1256/qj.04.01

The effect of upstream wind direction on atmospheric flow in the vicinity of a large mountain

By GUÐRÚN NÍNA PETERSEN[1,2]*, JÓN EGILL KRISTJÁNSSON[1]
and HARALDUR ÓLAFSSON[2,3]
[1]*University of Oslo, Norway*
[2]*University of Iceland, Reykjavik, Iceland*
[3]*Icelandic Meteorological Office and Institute for Meteorological Research, Iceland*

(Received 7 January 2004; revised 25 October 2004)

SUMMARY

A series of idealized simulations is conducted to investigate how the upstream wind direction impacts on the flow in the vicinity of a large elliptical mountain, oriented north–south. The upstream wind speed and stability are kept constant, there is no surface friction, the Rossby number is low and the non-dimensional mountain height, $\widehat{h} = Nh/U$, is varied from 1 to 4.5.

The flow pattern varies greatly with wind direction and a number of features of orographic flows where the Coriolis force is important are found. For a given $\widehat{h}$, the flow is blocked for low aspect ratio while it is not blocked for high aspect ratio. Furthermore, the upstream barrier wind is more pronounced when the upstream flow is from the south-west than from the north-west. Both these features are linked to the interaction of the Coriolis force with the mountain-induced flow anomalies. The drag force and the pressure deficit in the wake are greater in the south-west cases than in the north-west cases. These features are linked, as the main contribution to the drag being greater in the south-west cases is a negative pressure anomaly over the lee slope. The difference downstream of the mountain is linked to the interaction of the low-level flow anomalies and the Coriolis force.

KEYWORDS: Barrier jet Corner wind Greenland Low Rossby number Orographic blocking Orographic wake Surface pressure drag Tip jet

1. INTRODUCTION

Mountains can have a great impact on the atmospheric flow. Well-known examples are the middle tropospheric troughs created by the Rocky Mountains and the Tibetan Plateau. The impact is dependent on several parameters, such as the size and shape of the mountain, the wind speed and the stability of the atmosphere. Furthermore, the impact can vary in space. In the vicinity of mountains, regions can be found where the wind speed is increased locally, e.g. the tip jet (Doyle and Shapiro 1999). Downstream, in the lee of mountains, a wake can be generated with decreased wind speed or eddy shedding (Smith *et al.* 1997; Bauer *et al.* 2000), and gravity waves can be generated aloft (Smith *et al.* 2002).

The impact of mountains on atmospheric flow has been investigated in several studies. These studies have approached the investigation theoretically, numerically and/or have been based on observations in mountainous areas (e.g. Queney 1948; Eliassen and Palm 1960; Smith 1978, 1979; Bougeault *et al.* 1997; Ólafsson 2000). The impact of rotation on airflow past large mountains has received attention and so has the effect of surface friction (Ólafsson and Bougeault 1997; Hunt *et al.* 2001; Peng and Thompson 2003). Generally, studies of orographic impact concentrate on the immediate impact mountains have on the airflow, but long-term effects of mountain ranges such as Greenland have also been investigated (Petersen *et al.* 2004 and references therein; Orr *et al.* 2004). In most studies of simplified flow past mountains, the mountain is either circular or, in the case of an elongated mountain, the direction of the flow impinging upon the mountain remains the same. However, in nature the wind direction

* Corresponding author, present address: Department of Meteorology, University of Reading, Earley Gate, PO Box 243, Reading RG6 6BB, UK. e-mail: g.n.petersen@reading.ac.uk
© Royal Meteorological Society, 2005.

can vary greatly in time and space. The impact of the wind direction on the weather in southern Norway has been known for several decades (Spinnangr 1943a,b). Barstad (2002) confirmed that a relatively small perturbation in the upstream wind direction of airflow impinging upon southern Norway was important, e.g. for the placement of the downstream wake and the location and amount of precipitation in the region.

In this paper we wish to investigate how the upstream wind direction affects the atmospheric flow in the vicinity of a large mountain. We have conducted a series of simulations with three-dimensional flow over an elliptical mountain. The upstream vertical profile of wind and stability is constant while the wind direction is varied between simulations. The mountain is elliptical and has a half-length as Greenland and its half-width is comparable to southern Greenland. The height is varied and the flow pattern is investigated as well as the surface pressure drag in the zonal and meridional directions.

In the following section there is a short overview of the theory of simple flow, followed by a description of the numerical model and the parameters applied in the simulations. The results are described in section 4, a summary and discussion are found in section 5 and, finally, conclusions are given in section 6.

2. Theory of simple flow

When the conditions are right, the airflow impinging on a mountain can experience upstream blocking and/or wave breaking. Furthermore a tip jet can be found at the flanks of the mountain as well as a wake in the lee. Ólafsson and Bougeault (1996) defined upstream blocking as a mass of decelerated air upstream of the mountain with a partly reversed flow. Another approach is to define upstream blocking if there are one or more stagnation points on the windward slope, followed by flow splitting (Hunt and Snyder 1980). These definitions are difficult to apply in the present study since the upstream wind direction is varied and in each simulation the upstream flow experiences the mountain differently. The definition for upstream blocking that we have selected is as the other two definitions and involves the low-level flow; if the near-surface air is not able to flow over the top of the mountain, the flow is defined as blocked, otherwise it is unblocked. The wake is defined as the region downstream where there are eddies with recirculating flow, or a general deceleration. This definition was also applied in Petersen *et al.* (2003). Doyle and Shapiro (1999) defined the tip jet as the narrow low-level jet stream originating from the vertex of large elliptical barriers. This definition is applied in the present study.

A hydrostatic, inviscid, Boussinesq flow impinging on a mountain on a non-rotating plane is governed by the mountain shape, its aspect ratio, its non-dimensional mountain height, $\widehat{h} = Nh/U$, and the profile of the atmosphere (Smith and Grønås 1993). (See Table 1 for definitions.) According to Smith (1989a), a linear, frictionless, stratified flow impinging upon a mountain on a non-rotating plane can be divided into regimes according to information about the non-dimensional mountain height and the aspect ratio (his Fig. 5). The flow regimes are defined by the presence/absence of flow splitting and the presence/absence of wave breaking aloft. Ólafsson and Bougeault (1996) showed, through their numerical study, that nonlinear irrotational inviscid flow past an elongated mountain was in agreement with Smith's diagram. They also showed that, for a large $\widehat{h}$, the wave breaking region moves from the axis of symmetry to isolated areas on each side of the axis.

When the Coriolis force is included, the Rossby number, $Ro = U/fL_x$, enters as an additional parameter and the morphology of the flow changes. The left–right symmetry

TABLE 1. SUMMARY OF THE MOST IMPORTANT PARAMETERS IN THE SIMULATIONS

Parameter	Symbol	Value
Coriolis parameter	f	1.2×10^{-4} s^{-1}
Mountain half-length	L_y	800 km
Mountain half-width	L_x	200 km
Mountain (summit) height	h	(1000, 2000, 3000, 4500) m
Upstream wind speed	U	10 m s^{-1}
Upstream wind direction		(0, 360)°
Upstream Brunt–Väisälä frequency	N	0.01 s^{-1}
Rossby number	$Ro = U/fL_x$	0.42
Non-dimensional mountain height	$\widehat{h} = Nh/U$	(1.0, 2.0, 3.0, 4.5)

of the flow is broken and the flow is to a greater extent diverted to the left (facing downstream), giving greater wind speed than on the right-hand side of the mountain and delaying the onset of blocking (Pierrehumbert and Wyman 1985; Thorsteinsson and Sigurdsson 1996). A series of wind maxima resulting from inertia-gravity wave generation often exists in the northern part of the wake (Doyle and Shapiro 1999). In the study of Ólafsson and Bougeault (1997) on the effect of rotation and surface friction on flow past mountains, they found that for blocked flow the isentropes in the lee of the mountain were permanently deflected downwards and that the pressure deficit in the lee was reduced by the Coriolis force.

The impact of mountains on atmospheric flow can also be understood in terms of an orographic drag. Mountains extract momentum from the mean flow and thus affect the atmospheric momentum budget. This momentum is transferred to the earth at the surface, through surface friction and pressure gradient forces, expressed in terms of a pressure drag. The surface pressure drag is therefore an important sink of atmospheric momentum, and knowledge of its behaviour is essential for the large-scale momentum budget. It is also important to account for the impact of unresolved topography in numerical models, as has been the focus of several pressure drag studies (e.g. Lott and Miller 1997; Broad 1996; Shutts 1998; Brown and Wood 2001; Wood *et al.* 2001; Webster *et al.* 2003). An overview of orographic drag parametrizations in numerical models can be found in Kim *et al.* (2003).

Ólafsson and Bougeault (1997) investigated the effect of rotation and surface friction on orographic drag when $Ro = 2.5$. They found rotation to have different effects on blocked and unblocked flow. In unblocked flow (high-drag regime) the Coriolis force decreased the drag of large-amplitude breaking waves while it increased the orographic drag and brought it closer to its linear value in blocked flow (low-drag regime). Ólafsson (2000) continued this work by investigating how the drag asymmetry is affected by the flow regime and the Rossby number. He found the drag to be larger on the left flank of the mountain (facing downstream) than on the right flank when the flow was unblocked, i.e. the mountain exerts a cyclonic drag asymmetry on the atmosphere. When the flow is blocked, it is the drag on the right flank which is larger and the mountain exerts an anticyclonic drag asymmetry on the atmosphere (see his Fig. 13).

3. THE EXPERIMENTAL SET-UP

The experimental set-up is the same as in Petersen *et al.* (2003), with the exception that in the present study we vary the wind direction but maintain the same wind speed and stability throughout the simulations.

The third version of the mesoscale model MM5 from Penn State/NCAR* is applied (Grell *et al.* 1995). It is a non-hydrostatic sigma-coordinate model designed to simulate or predict mesoscale and regional-scale circulation. It has been used for a broad spectrum of theoretical as well as real-time studies.

A second-order leapfrog time-stepping scheme is applied, but some terms in the basic equations are handled using a time-splitting scheme. The time step in the experiments is 90 seconds.

The horizontal grid has an Arakawa–Lamb B-staggering of the velocity components with respect to the scalars. The idealized experiments presented here have all been run with a 36 km horizontal grid spacing and 150×150 grid points in the horizontal. In the vertical there are 40 σ-levels, where the σ-coordinate is defined by

$$\sigma = \frac{p - p_t}{p_s - p_t}. \tag{1}$$

Here, p is the pressure, p_t is a specified constant top pressure (10 hPa) and p_s is the surface pressure. To prevent wave reflection, a Rayleigh damping layer, which is not a standard parametrization in MM5, is included. The layer is placed above 13 km height, and the wave absorption coefficient increases with height. In the simulations the atmosphere is simple; neither humidity nor radiation are included. A high concentration of turbulent kinetic energy and steep isentropes are major criteria for detection of wave breaking, as in Ólafsson and Bougeault (1996), for example. Thus from the planetary boundary-layer schemes available, a scheme which predicts turbulent kinetic energy for use in vertical mixing (Burk and Thompson 1989), and based on the Mellor–Yamada formulae (Mellor and Yamada 1982), was chosen. The turbulent fluxes at the lowest σ-level were set to zero, to enable the use of free slip at the lower boundary.

The mountain in the experiments is bell-shaped, with height given by

$$H(x, y) = \frac{h}{\{1 + (x/L_x)^2 + (y/L_y)^2\}^{1.5}} \tag{2}$$

where L_x and L_y are respectively the mountain half-width in the east–west direction and the half-length in the north–south direction. Here we set L_x to 200 km and L_y to 800 km, which gives us a mountain of similar size to Greenland. The aspect ratio is defined as the mountain width perpendicular to the flow direction divided by the width in the flow direction. Consequently, for a westerly wind the aspect ratio is $r = L_y/L_x = 4$ while for northerly flow it is $r = L_x/L_y = 0.25$. The Coriolis parameter is set to a value representative for about 55°N. The model is initialized everywhere with the horizontal wind speed $U = 10$ m s^{-1} and the upstream Brunt-Väisälä frequency $N = 0.01$ s^{-1}. The Rossby number, $Ro = U/fL_x$, is 0.42. The non-dimensional mountain height, $\widehat{h} = Nh/U$, is then varied by changing the mountain height. Thus, a high $\widehat{h}$ represents a high mountain. Also, because the half-length and half-width of the mountain are held constant, a higher mountain is steeper than a lower mountain. The height of the mountain is varied between 1000 m and 4500 m and thus the non-dimensional height varies from 1.0 to 4.5. The wind direction is varied from 0° to 360° at intervals of 30°. Table 1 gives an overview of the most important parameters.

The surface pressure drag that is due to the pressure anomalies around the mountain and is exerted on the mountain in the zonal direction can be written as

$$\mathcal{D} = \int_0^\infty \int_0^\infty p'(x, y) \frac{\partial H(x, y)}{\partial x} \, \mathrm{d}x \, \mathrm{d}y, \tag{3}$$

* Pennsylvania State University/National Center for Atmospheric Research.

where p' is the surface pressure anomaly, which is a result of the flow impinging on the mountain. If there is a pressure gradient in the background flow, there is an additional contribution to the drag force, but in most of the remainder of this paper only drag due to the mountain-induced pressure anomalies will be considered. The force on the atmosphere is equal but in the opposite direction. In this paper we will consider the drag positive when the flow has a westerly component. The term 'centre drag' is applied in the paper for the surface pressure drag calculated along the centre line of the mountain, while the term 'total drag' is applied for the surface pressure drag integrated over the whole mountain. Here we calculate the surface pressure drag only in the zonal and meridional directions. The drag produced in non-rotating conditions by an infinite, two-dimensional bell-shaped mountain on a slice of the flow of width L_y is given by

$$\mathcal{D}_{\mathrm{2D,lin}} = \tfrac{1}{4}\pi\rho_o N U h^2 L_y, \tag{4}$$

where ρ_o is the mean density. This formula is valid for flow around a mountain described by Eq. (2), but with 1 (and not 1.5) as exponent in the denominator. The surface pressure drag calculated in the present study will be normalized by Eq. (4), applying $\rho_o = 1.2$ kg m^{-3} and setting L_y equal to a unit width in the normalization of the centre drag but equal to the mountain half-length in the normalization of the total surface drag.

The model was run for 336 hours or 60.48 non-dimensional time units ($t^* = Ut/L_x$) in all the simulations. The initial perturbations have advected far beyond the mountain in all the simulations after about $t^* \approx 34$. Due to this dependence on the initial condition close to the mountain during the first 34 non-dimensional time units, this time interval is regarded as spin-up and is not included in the mean values.

4. Results

The flow pattern in the simulations varies greatly. When $\widehat{h} = 1.0$, mountain waves are found over the lee side but there is no wave breaking. For larger $\widehat{h}$, the flow experiences either wave breaking aloft, upstream blocking or both, depending on $\widehat{h}$ and the upstream wind direction. A diagram of the flow regimes is presented in Fig. 1. The diagram shows the regimes for upstream wind direction from southerly clockwise to northerly. The regime diagram for southerly anticlockwise to northerly is exactly the same and therefore is not shown. When the flow is from the south or north, the aspect ratio of the mountain is $r = L_x/L_y = 0.25$. As $\widehat{h}$ is increased from 1 to 4.5, the flow changes from the mountain-wave regime to the upstream-blocking regime, the flow becoming mainly horizontal. However, when the upstream flow is from the west, the aspect ratio is 4. Here, as $\widehat{h}$ is increased the flow changes regimes from the mountain-wave regime, through the wave-breaking regime to the regime of upstream blocking and wave breaking. When the wind direction is not from the cardinal points, the regime shift with increasing $\widehat{h}$ is similar to the one for wind from west or east. That is, when the flow is not from north or south the flow experiences a mountain of aspect ratio greater than one. An asymmetry is found in the shift from the wave-breaking regime to a regime with both wave breaking and upstream blocking; at $\widehat{h} = 3.0$ the flow experiences only wave breaking for upstream wind from west-south-west and west, while for other wind directions both wave breaking and upstream blocking are present.

Figure 2 shows the sea level pressure when $\widehat{h} = 3.0$ for two upstream wind directions at $t^* = 60.48$; west-south-west (240°) and west-north-west (300°). The surface low seen in the wake in Fig. 2(a) is shedding downstream while the low in Fig. 2(b) is almost stationary. In the case of an upstream wind from west-north-west, the pressure

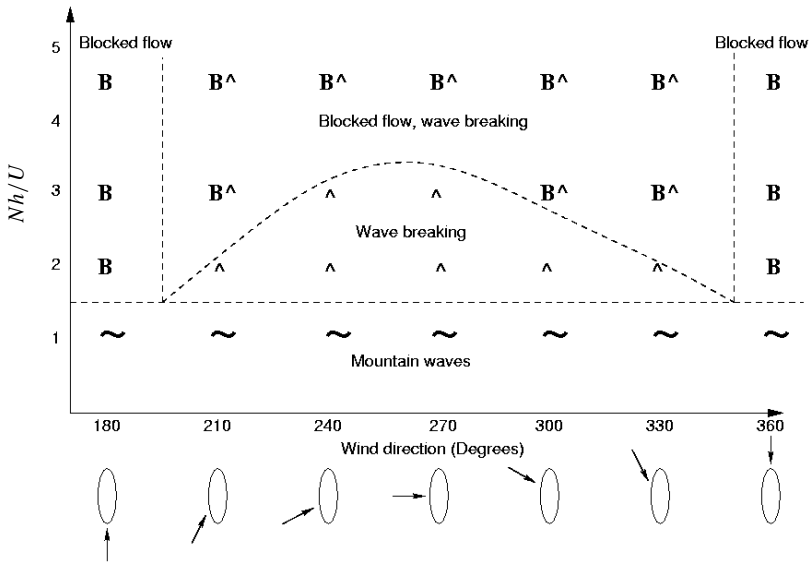

Figure 1. Diagram showing the flow regime as a function of non-dimensional mountain height, $\widehat{h} = Nh/U$, and the upstream wind direction.

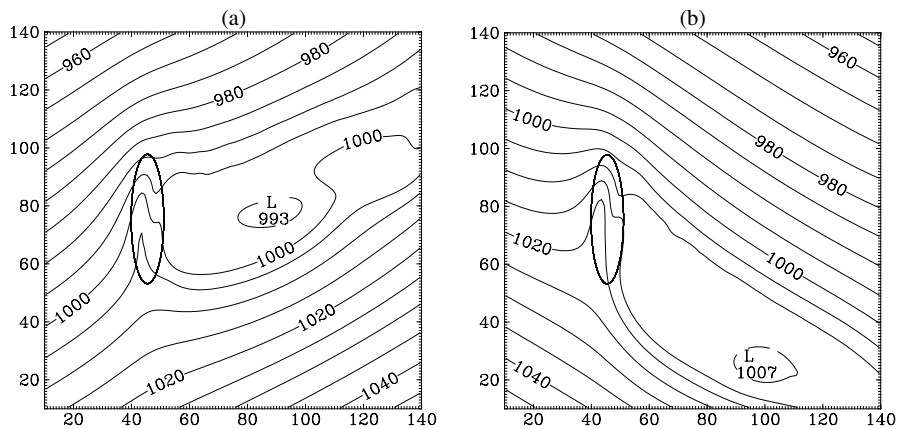

Figure 2. Sea-level pressure (contour interval 5 hPa) at time $t^* = 60.48$ for upstream airflow from (a) west-south-west and (b) west-north-west. The non-dimensional mountain height $\widehat{h} = 3$, the mountain is shown at $0.35h$, and the axes are grid point indices.

gradient upstream of the mountain is weaker than in the west-south-west case and there is little eddy shedding in the wake. The wind speed at the lowest σ-level also shows this dependence on wind direction (Fig. 3). In the west-north-west case, the wind speed decreases to half its initial value over the south-western slope and the wind direction becomes southerly. On the other hand, downstream of the southern tip there is a clearly defined tip jet with maximum wind speed exceeding twice the upstream wind speed. In the west-south-west case, the wind speed over the western slope does not decrease as much as the flow impinges upon the mountain. However, there is an increase in the wind speed as the air flows northwards approximately parallel to the west slope of the mountain, that is, a pronounced barrier wind. North of the wake there is a series of wind

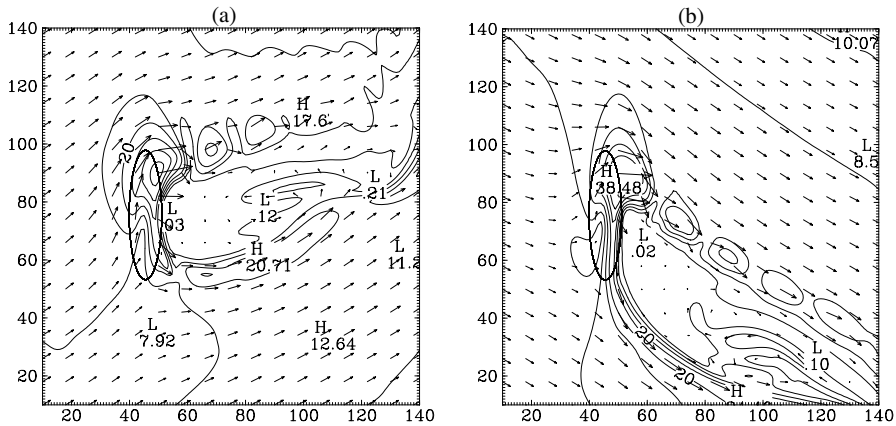

Figure 3. As Fig. 2, but showing wind speed (contour interval 5 m s^{-1}) and wind vectors at the lowest σ-level.

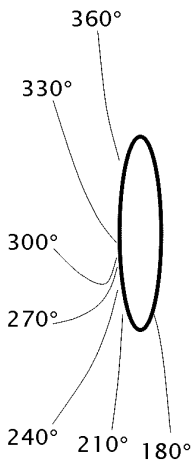

Figure 4. The dividing streamline between air flowing to the north and to the south of the mountain for the indicated upstream wind directions when the non-dimensional mountain height $\widehat{h} = 3.0$. The mountain height is shown at $0.35h$.

maxima resulting from inertia-gravity waves. These wind maxima are stationary and probably very sensitive to the shape of the mountain. They will not be discussed further in this paper.

Some of these features cannot be found in the simulations with other values of $\widehat{h}$. For $\widehat{h} = 4.5$ (not shown), there is more eddy shedding in the wake for both wind directions, the tip jet is not as well defined with west-north-westerly upstream wind as for $\widehat{h} = 3.0$, and there is a closer connection between the tip jet and the lows that shed through the wake. In $\widehat{h} = 2.0$ the wake is narrow with no eddy shedding and the wind on the southern side of the wake is constant in time. The dividing streamline between air flowing to the north of the mountain top and to the south of it shows that a larger air mass flows along the western slope of the mountain with south-westerly wind directions than with north-westerly wind directions, in which case the air is forced to change direction significantly (Fig. 4).

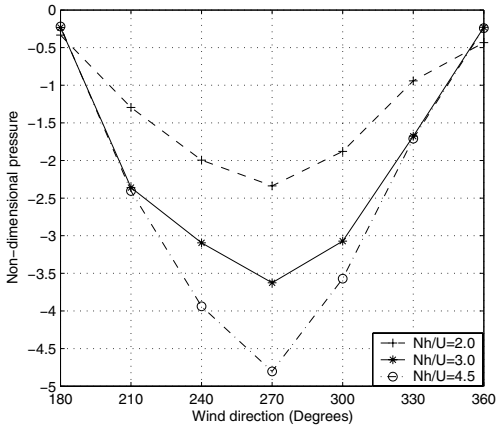

Figure 5. The non-dimensional sea-level pressure deficit in the wake as a function of wind direction for three values of non-dimensional mountain height, $\widehat{h} = Nh/U$. The pressure is normalized with $\rho_o NUh$.

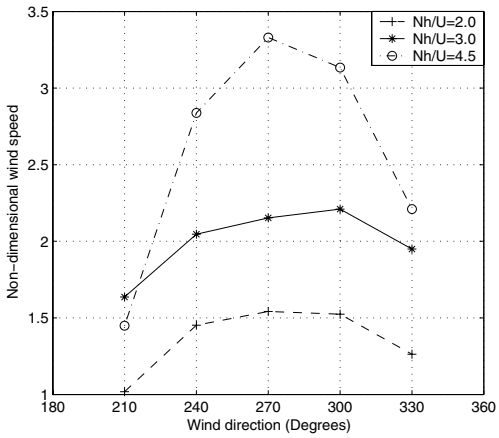

Figure 6. The non-dimensional wind speed in the tip jet as a function of wind direction for three values of non-dimensional mountain height, $\widehat{h} = Nh/U$. The wind speed is normalized with U.

Figure 5 shows the mean maximum sea level pressure deficit in the wake as a function of the upstream wind direction and the mountain height. Not unexpectedly, the pressure deficit increases with increased mountain height. The maximum pressure deficit is found for upstream wind from the west. When the upstream wind direction deviates from westerly, there is an asymmetry in the impact on the pressure. The pressure deficit is larger for deviations to the south than to the north, resulting in a deeper wake.

An inspection of the wind speed in the tip jet shows that the strength of the tip jet is highly dependent on the mountain height (see Fig. 6). Also for $\widehat{h} = 4.5$ ($h = 4500$ m) there is a strong variation in the strength of the tip jet depending on the wind direction. When $\widehat{h} = 2.0$ it is difficult to define the tip jet and for $\widehat{h} = 1.0$ (not shown), the tip jet is practically non-existent. The variation in the strength with mountain height is largest for a westerly upstream wind and least when the upstream wind approaches from the north or south. For upstream flow from the north or south, the tip jet is ill-defined and therefore not shown.

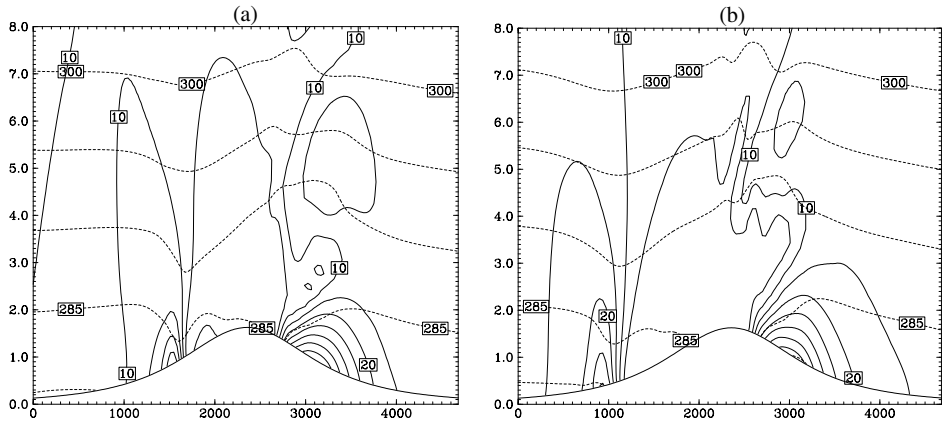

Figure 7. Wind speed (solid, contour interval 5 m s^{-1}) and potential temperature (dashed, interval 5 K) at time $t^* = 60.48$ in a south–north cross-section one half-width east of the mountain crest for (a) west-south-westerly and (b) west-north-westerly upstream wind impinging on a mountain with $\widehat{h} = 4.5$.

Figure 7 shows the wind speed and potential temperature in a cross-section along the y-axis over the lee slope when $\widehat{h} = 4.5$. The figure reveals that the jet emanating from the southern tip of the mountain is much narrower than the corner wind on the northern flank. The location and the intensity of the corner winds are similar in the west-south-west and west-north-west cases, while the tip jet off the southern tip is much farther south and of greater intensity in the west-north-west case.

Figure 8 shows a comparison of the pressure perturbations due to the mountain, as a function of the wind direction, in the west–east centre section of the mountain ($y = 0$) and in cross-sections $0.5L_y$ to the left (north) and right (south) of the centre section. Upstream, the pressure anomaly is smaller over the right flank than over the centre and the left flank of the mountain. When the upstream wind direction is changed from west-south-west (Fig. 8(a)) to west-north-west (Fig. 8(c)), the anomaly over the upstream left flank increases by about 0.26 non-dimensional pressure units (1 hPa), while the anomaly over the upstream right flank decreases by about 0.13 non-dimensional pressure units (0.5 hPa). Downstream, the pressure pattern varies. For upstream airflow from west-south-west, the wake is mainly to the east of the mountain and all the cross-sections show negative pressure anomalies. The anomaly over the right flank is of similar size to that at the centre section of the mountain, but the maximum anomaly is located closer to the mountain than at the centre section. For upstream westerly flow, the wake is mainly located in the lee of the southern part (right-hand side), while the wake is almost entirely south of the mountain for west-north-westerly upstream flow and can only be detected in the pressure perturbation over the right flank, close to the mountain.

Figure 9(a) shows the pressure perturbations along the west–east centre line for the three wind directions mentioned. Upstream the wind direction has little effect but downstream there are large differences and the anomaly has the largest value for upstream west-south-westerly wind, with almost -3 non-dimensional pressure units (-11 hPa). Figure 9(b) shows the pressure perturbations along the south–north centre section for the same wind directions. In contrast to westerly and west-south-westerly wind directions, where the air piles up over the southern flank of the mountain, there is a pressure deficit to the south in west-north-westerly winds due to the flow being diverted northwards.

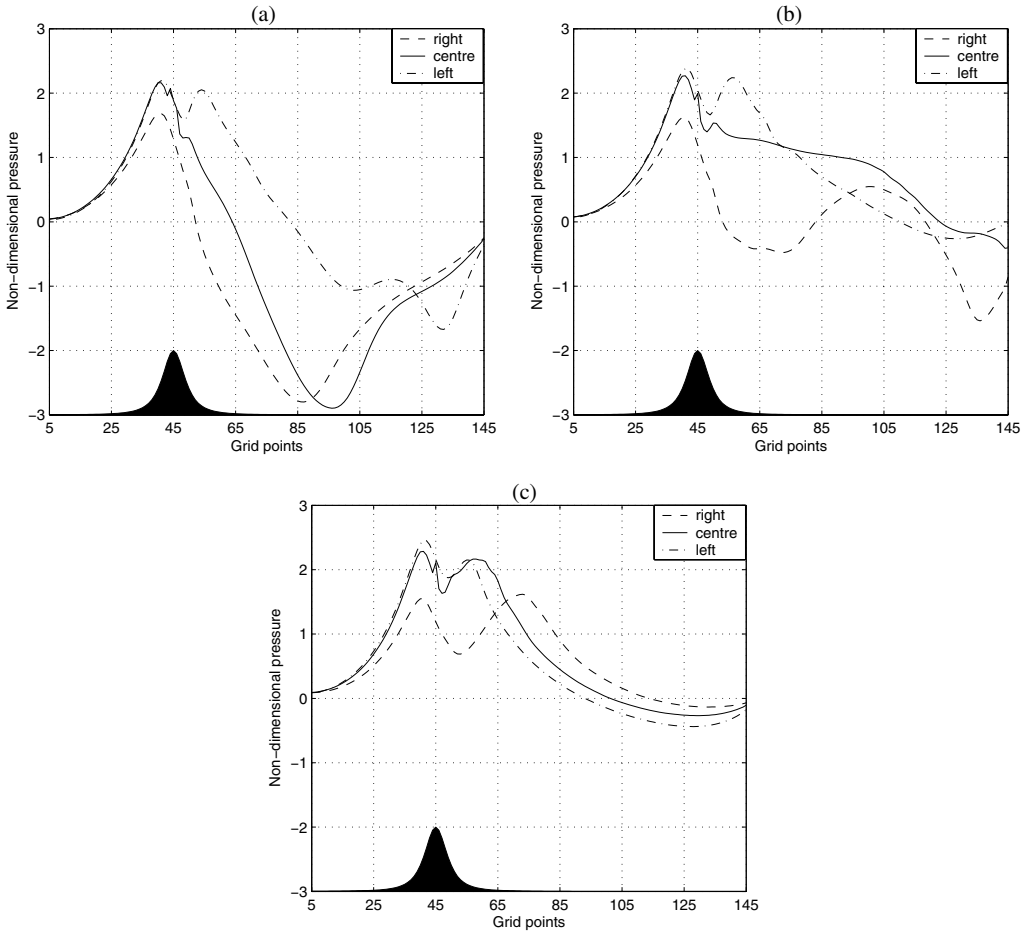

Figure 8. Pressure perturbations at time $t^* = 60.48$ along a section 0.5 L_y to the right of the west–east centre line of the mountain, along the centre line and 0.5 L_y to the left of the centre line for (a) west-south-westerly, (b) westerly and (c) west-north-westerly upstream winds impinging on a mountain with $\widehat{h} = 3.0$. The pressure is normalized with $\rho_o NUh$, and the mountain profile is shown at the bottom.

Figure 10 shows the non-dimensional zonal surface pressure drag along the west–east symmetry axis of the mountain and the non-dimensional zonal total surface pressure drag. The figure shows that the behaviour of the symmetry axis section drag is similar to the behaviour of the total pressure drag. Opposite wind directions have drag of the same value but with reverse sign. The behaviour of the drag force in all three cases when there is upstream blocking and/or wave breaking ($\widehat{h} \geqslant 2.0$) is similar, while in the case of only mountain waves ($\widehat{h} = 1.0$) the drag behaves differently. Here, the drag has lower maximum and minimum values and the extremes are found at wind directions from the east or the west. In the other cases, the extremes are not found for upstream wind perpendicular to the longer side of the mountain but for a wind direction diverted slightly anticlockwise. The meridional surface pressure drag along the south–north symmetry axis of the mountain has the same pattern, the extremes being diverted anticlockwise from the south/north wind direction (see Fig. 11).

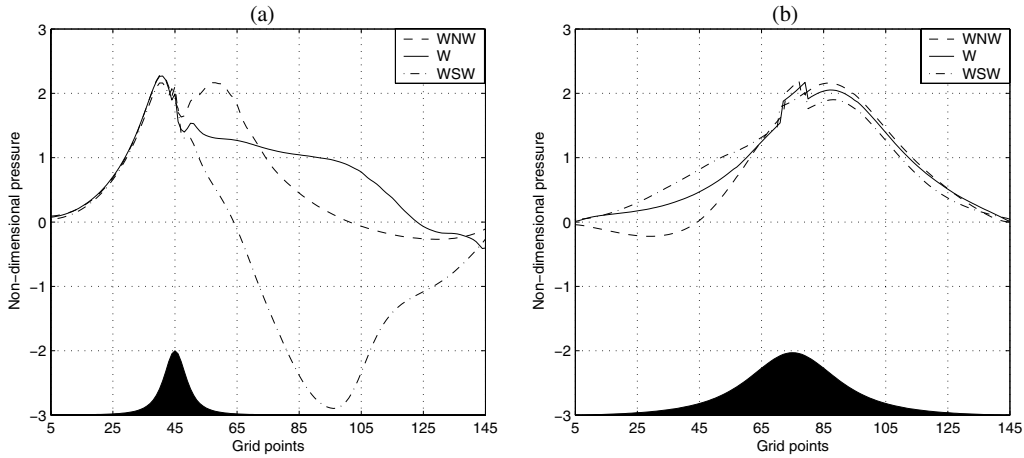

Figure 9. Pressure perturbations at time $t^* = 60.48$ along (a) the west–east centre line and (b) the south–north centre line of the mountain for upstream wind from west-south-west, west and west-north-west impinging on a mountain with $\widehat{h} = 3.0$. The pressure is normalized with $\rho_o NUh$, and the mountain profile is shown at the bottom.

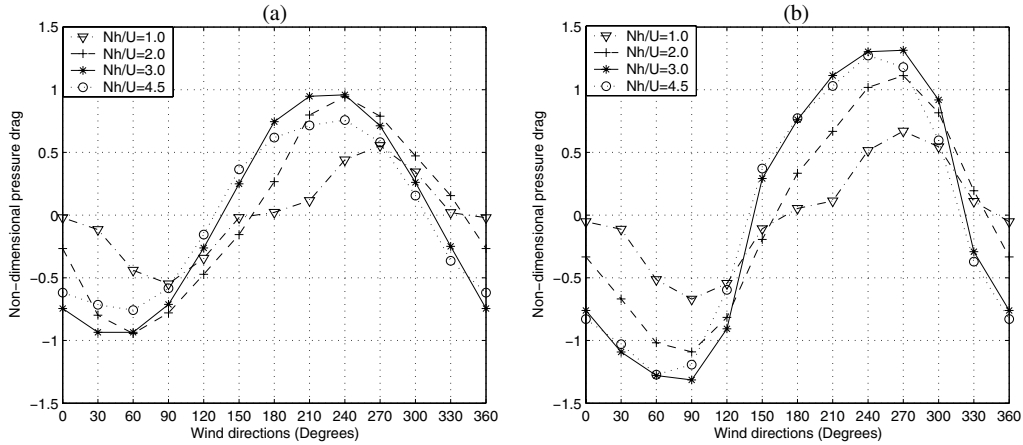

Figure 10. Non-dimensional (a) zonal surface pressure drag along the west–east centre section of the mountain and (b) total zonal surface pressure drag, as a function of wind direction for different values of $\widehat{h} = Nh/U$. The drag is normalized with $\pi\rho_o NUh^2 L_y/4$, where L_y is a unit width in (a) and the mountain half-length in (b).

The pressure field can be divided into the background geostrophic flow and the pressure perturbations created as the flow impinges on the mountain. So far, we have only shown results for the pressure perturbations, omitting the contribution of the background flow to the drag. Figure 12 shows the drag due to the background flow together with the drag due to the pressure perturbations and the sum of the two for $\widehat{h} = 3.0$ along the west–east centre section. As expected, the drag due to the background flow is symmetric about its minimum in flow from the south, while the drag due to the pressure perturbations has a minimum in north-easterly flow and a maximum in south-westerly flow. The total of the two drag contributions features an anticlockwise shift of the drag compared to the background flow.

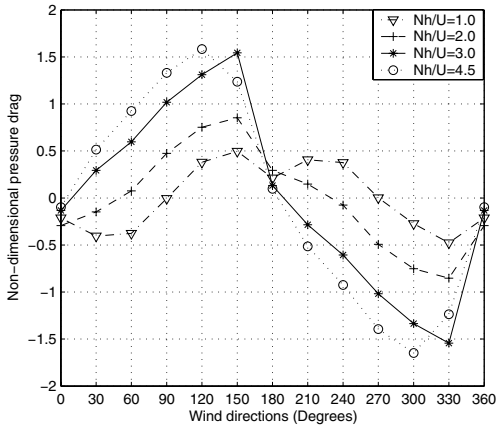

Figure 11. Non-dimensional meridional surface pressure drag along the south–north centre section of the mountain as a function of wind direction for different values of $\widehat{h}$. The drag is normalized with $\pi\rho_o NUh^2 L_y/4$, where L_y is a unit width.

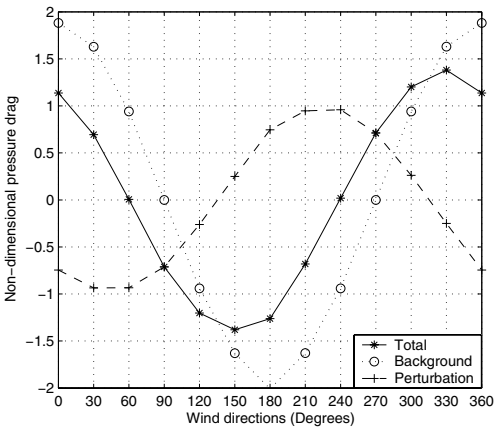

Figure 12. Non-dimensional surface pressure drag along the west–east centre section of the mountain as a function of wind direction for $\widehat{h} = 3.0$: total surface pressure drag (solid), the contributions from the background flow (dotted) and the mountain-induced pressure perturbations (dashed). The drag is normalized with $\pi\rho_o NUh^2 L_y/4$, where L_y is a unit width.

5. Discussion

The simulations conducted in this investigation were carried out with constant upstream stability and wind speed while the wind direction was varied between simulations. The mountain was bell-shaped, its half-length and half-width were kept constant but the mountain height varied. There was no surface friction and neither humidity nor radiation was included in the simulations.

The simulations presented in this paper reveal a number of new features of orographic flows where the Coriolis force is important. These features are mainly related to elements of the flow associated with its nonlinear character and are therefore not within the frame of the quasi-geostrophic flow as described by Queney (1948). However, most of these elements such as the upstream barrier jet and the asymmetric wake are described for zonal wind in the analytic model of Hunt *et al.* (2001).

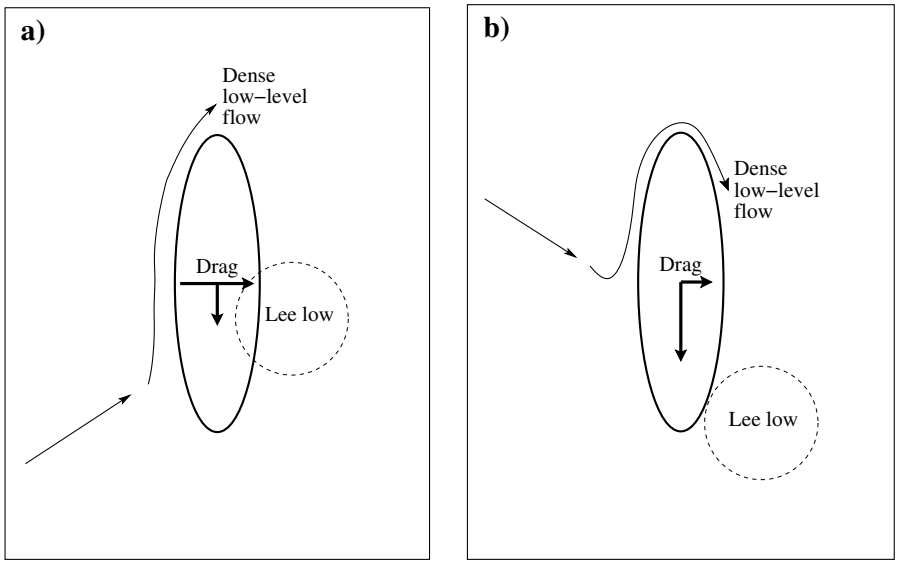

Figure 13. Schematic illustration of the flow and surface pressure drag in (a) west-south-westerly and (b) west-north-westerly upstream wind directions. The thin arrows represent streamlines and the bold vectors represent the surface pressure drag due to the mountain. (The drag vectors show the drag on the mountain; that on the atmosphere is of opposite sign. The length of the drag vectors only represents the difference of drag between the two wind directions. The zonal drag vectors should not be compared to the meridional drag vectors.)

On the upstream side, the variation of the orographic response of the flow to variation in upstream wind direction includes two interesting aspects. Firstly, for a certain range of $\widehat{h}$, the flow is blocked for low aspect ratio while for higher aspect ratio, the flow is not blocked. This contradicts the results of irrotational linear theory, where the flow is more easily blocked upstream of mountains with high aspect ratio (Smith 1989b). Secondly, a strong barrier wind is created along the upstream slope in the case of flow from the west-south-west, while if the flow is from the west-north-west, the increase in wind speed along the upstream slope is much less pronounced. Both these features can be explained by considering how the Coriolis force interacts with the mountain-induced flow anomalies. The barrier wind along the upstream slope in the cases of flow from the south-west can be viewed as a consequence of the flow turning to the left as it approaches the mountain, decelerating and the Coriolis force weakening. In the south-west cases, turning to the left directs the flow along the upstream slope while in the north-west cases turning to the left directs the flow towards the mountain (Fig. 13). In the case of low aspect ratio, this diversion to the left is small since the upstream wind direction is parallel to the longer mountain side. On the other hand, in the case of high aspect ratio, the Coriolis force causes the flow to travel along the entire lee slope. Here, the Coriolis force pulls the flow for a long distance towards the mountain and up the slopes, helping the low-level air mass to ascend the highest part of the mountain.

The zonal drag force and the pressure deficit in the wake are greater in the south-west cases than in the north-west cases. These features are intimately linked since the negative pressure anomaly over the lee slope is the main contribution to the drag being greater in the south-west cases. The low pressure in the wake is associated with air masses that have descended downstream of the mountain. This descent is forced by continuity as the low-level flow is pulled away from the mountain by the pressure gradient between the northern and the southern edge of the mountain, acting together

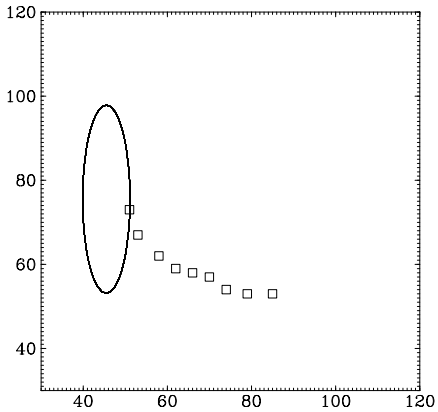

Figure 14. The temporal evolution of the position of the maximum sea level pressure anomaly downstream of the mountain in westerly flow. The squares indicate the position at 2, 6, 12, 18, 24, 30, 36, 42 and 48 hours of simulation. The mountain is shown at $0.35h$.

with the Coriolis force. In the south-west cases, the low-level dense air piles up at the southern tip of the mountain, while in the north-west cases, there is more pronounced piling up of dense air at the northern tip of the mountain (Figs. 7 and 9(a)). Thus, the mountain-induced pressure gradient between its northern and southern flanks adds to the background pressure gradient in the south-west cases, while in the north-west cases the mountain-induced pressure gradient contributes to the reduction of the large-scale gradient. The pulling away of low-level air immediately downstream of the mountain is in other words more efficient in the south-west cases. The shearline is sharper and the tip jet is stronger in the north-west cases than in the south-west cases. Here, there is no obvious dynamic explanation, but we expect asymmetry to be associated with the shape of the mountain; the tip jet in the north-westerly flow has a stronger meridional component than the tip jet in the south-westerly flow and the mountain is steeper in the zonal than in the meridional direction. For steep slopes, the shearline can be expected to be sharper and the wind speed to be stronger than for gentle slopes (Barstad 2002).

The drag being greater in the south-west cases than in the north-west cases is also related to the wake being positioned much closer to the central part of the mountain in the south-west cases (see Fig. 13). The position of the wake with respect to the mountain is different in the different simulations, but its position with respect to a line crossing the mountain top and running parallel to the upstream flow is roughly the same in all cases. It was expected to find the wake directly downstream of the highest part of the mountain and its deflection to the right (south) needs to be explained. Geostrophic adjustment of the flow to a low pressure anomaly in the lee of the mountain results in flow away from the mountain to the south of the low and flow towards the mountain to the north of the low. A potentially warm and light air mass is consequently pulled downwards over the lee slopes on the right-hand (south) side of the mountain. The circulation generated by the lee low thus contributes to moving the low itself further south. An investigation of the early evolution of the flow in the simulation with upstream wind from the west confirms this concept. Figure 14 shows the position of the low during the first 48 hours of the simulation. At the very beginning of the simulation, the low is close to being downstream of the mountain top, while 12 hours later it has moved much further south.

6. Conclusions

The topic of the present study is the interaction between a large mountain and the flow at different flow directions. The simulations show the interaction between the Coriolis force and the upstream wind direction to be important. Upstream of the mountain, the Coriolis force acts to enhance flow from the south-west, working with the upstream wind direction resulting in a pronounced barrier wind, while it acts to weaken flow from the north-west, turning the flow to southerly. Downstream, the position and depth of the lee wake is dependent on the interaction of the Coriolis force and the low-level flow anomalies, resulting in a shallower wake and a smaller surface pressure drag in the north-west cases than in the south-west cases.

In our simulations, there is a general tendency towards a larger difference between south-westerly and north-westerly flows as $\widehat{h}$ increases. This agrees with the fact that, for increasing $\widehat{h}$, the flow enters further into the blocked regime and, in our interpretation of the asymmetries in the flow, blocking and lateral diversion of the low-level flow is the key factor.

Acknowledgements

This research is partly financed by the Research Council of Norway (grant 133634/432). The authors would like to thank the reviewers for valuable comments and suggestions.

References

Barstad, I. 2002 'Southwesterly flows over southern Norway'. PhD thesis, University of Bergen, Norway

Bauer, M. H., Mayr, G. J., Vergeiner, I. and Pichler, H. 2000 Strongly nonlinear flow over and around a three-dimensional mountain as a function of the horizontal aspect ratio. *J. Atmos. Sci.*, **57,** 3971–3991

Bougeault, P., Benech, B., Bessemoulin, P., Carissimo, B., Jansa Clar, A., Pelon, J., Petitdidier, M. and Richard, E. 1997 PYREX: A summary of findings. *Bull. Am. Meteorol. Soc.*, **78,** 637–650

Broad, A. S. 1996 High-resolution numerical-model integration to validate gravity-wave-drag parametrization schemes: A case-study. *Q. J. R. Meteorol. Soc.*, **122,** 1625–1653

Brown, A. R. and Wood, N. 2001 Turbulent form drag on anisotropic three-dimensional orography. *Boundary-Layer Met*, **101,** 229–241

Burk, S. D. and Thompson, W. T. 1989 A vertically nested regional numerical weather prediction model with second-order closure physics. *Mon. Weather Rev.*, **117,** 2305–2324

Doyle, J. D. and Shapiro, M. A. 1999 Flow response to large-scale topography: the Greenland tip jet. *Tellus*, **51A,** 728–748

Eliassen, A and Palm, E. 1960 On the transfer of energy in stationary mountain waves. *Geophys. Norv.*, **22,** 1–23

Grell, G. A., Dudhia, J. and Stauffer, D. R. 1995 'A description of the fifth-generation Penn State/NCAR mesoscale model (MM5)'. Technical Note 398+STR, NCAR, Boulder, USA

Hunt, C. R. and Snyder, W. H. 1980 Experiments on stably and neutrally stratified flow over a model three-dimensional hill. *J. Fluid Mech.*, **96,** 671–704

Hunt, J. C. R., Ólafsson, H. and Bougeault, P. 2001 Coriolis effects on orographic and mesoscale flows. *Q. J. R. Meteorol. Soc.*, **127,** 601–633

Kim, Y.-J., Eckermann, S. D. and Chun, H.-Y. 2003 An overview of the past, present and future gravity-wave drag parameterization for numerical climate and weather prediction models. *Atmosphere-Ocean*, **41,** 65–98

Lott, F. and Miller, M. J. 1997 A new subgrid-scale orographic drag parametrization: Its formulaton and testing. *Q. J. R. Meteorol. Soc.*, **123,** 101–127

Mellor, G. L. and Yamada, T. 1982 Development of a turbulence closure model for geophysical fluid problems. *Rev. Geophys. Space Phys.*, **20,** 851–875

Ólafsson, H. 2000 The impact of flow regimes on asymmetry of orographic drag at moderate and low Rossby numbers. *Tellus*, **52A,** 365–379

Ólafsson, H. and Bougeault, P. 1996 Nonlinear flow past an elliptic mountain ridge. *J. Atmos. Sci.*, **53,** 2465–2489

1997 The effect of rotation and surface friction on orographic drag. *J. Atmos. Sci.*, **54,** 193–209

Orr, A., Cresswell, D., Marshall, G. J., Hunt, J. C. R., Sommeria. J., Wang, C. G. and Light, M. 2004 A 'low level' explanation for the recent large warming trend over the western Antarctic Peninsula involving blocked winds and changes in zonal circulation. *Geophys. Res. Lett.*, **31**(6), L06204

Peng, M. S. and Thompson, W. T. 2003 Some aspects of the effect of surface friction on flows over mountains. *Q. J. R. Meteorol. Soc.*, **129,** 2527–2557

Petersen, G. N., Ólafsson, H. and Kristjánsson, J. E. 2003 Flow in the lee of idealized mountains and Greenland. *J. Atmos. Sci.*, **60,** 2183–2195

Petersen, G. N., Kristjánsson, J. E. and Ólafsson, H. 2004 Numerical simulations of Greenland's impact on the Northern Hemisphere winter circulation. *Tellus*, **56A,** 102–111

Pierrehumbert, R. T. and Wyman, B. 1985 Upstream effects of mesoscale mountains. *J. Atmos. Sci.*, **42,** 977–1003

Queney, P. 1948 The problem of the airflow over mountains. A summary of theoretical studies. *Bull. Am. Meteorol. Soc.*, **29,** 16–26

Doyle, J. D. and Shapiro, M. A. 1999 Flow response to large-scale topography: the Greenland tip jet. *Tellus*, **51A,** 728–748

Shutts, G. 1998 Idealized models of the pressure drag force on mesoscale mountain ridges. *Contrib. Atmos. Phys.*, **71,** 303–346

Smith, R. B. 1978 A measurement of mountain drag. *J. Atmos. Sci.*, **35,** 1644–1654

1979 The influence of the earth's rotation on mountain wave drag. *J. Atmos. Sci.*, **36,** 177–180

1989a Hydrostatic airflow over mountains. *Adv. Geophys.*, **31,** 59-81

1989b Mountain-induced stagnation points in hydrostatic flow. *Tellus*, **41A,** 270–274

Smith, R. B., Gleason, A. C., Gluhosky, P. A. and Grubišić, V. 1997 The wake of St. Vincent. *J. Atmos. Sci.*, **54,** 606–623

Smith, R. B. and Grønås, S. 1993 Stagnation points and bifurcation in 3-D mountain airflow. *Tellus*, **45A,** 28–43

Smith, R. B., Skubis, S., Doyle, J. D., Broad, A. S., Kiemle, C. and Volkert, H. 2002 Mountain waves over Mont Blanc: Influence of a stagnant boundary layer. *J. Atmos. Sci.*, **59,** 2073–2092

Spinnangr, F. 1943a Synoptic studies on precipitation in southern Norway. I. Instability showers. *Meteorol. Ann.*, 323–356

1943b Synoptic studies on precipitation in southern Norway. II. Front precipitation. *Meteorol. Ann.*, 433–468

Thorsteinsson, S. and Sigurdsson, S. 1996 Orogenic blocking and deflection of stratified air flow on an f-plane. *Tellus*, **48A,** 572–583

Webster, S., Brown, A. R., Cameron, D. R. and Jones, C. P. 2003 Improvement to the representation of orography in the Met Office Unified Model. *Q. J. R. Meteorol. Soc.*, **129,** 1989–2010

Wood, N., Brown, A. R. and Hewer, F. E. 2001 Parametrizing the effects of orography on the boundary layer: An alternative to effective roughness lengths. *Q. J. R. Meteorol. Soc.*, **127,** 759–777